Journal of
Intelligent Material
Systems and Structures

Article

Journal of Intelligent Material Systems and Structures
23(14) 1649–1658

DOI: 10.1177/1045389X12449921
jim.sagepub.com
SAGE

Enhancement of the magnetoelectric coefficient in functionally graded multiferroic composites

Jan Sladek[1], Vladimir Sladek[1], Slavomir Krahulec[1] and Ernian Pan[2]

Abstract

A meshless method based on the local Petrov–Galerkin approach is proposed to solve static and dynamic problems in functionally graded magnetoelectroelastic plates. Material properties on the bottom surface have a pure piezomagnetic behavior, and on the top surface, they are pure piezoelectric. Along the plate thickness, the material properties are continuously varying. The magnetoelectric coefficient is vanishing in pure piezoelectric as well as in pure piezomagnetic constituents. It is shown, however, that a finite electric potential in the functionally graded composite can be induced by an applied magnetic potential. It means that a finite magnetoelectric coefficient exists in a functionally graded composite plate made of different phases with vanishing magnetoelectric coefficients. It is a way to enhance the magnetoelectric coefficient in composites. Various gradations of material coefficients are considered to analyze their influence on the magnitude of magnetoelectric coefficients. Pure magnetic and combined magnetic–mechanical loads are analyzed. The meshless local Petrov–Galerkin is developed for the solution of boundary value problems in magnetoelectroelastic solids with continuously varying material properties.

Keywords

meshless local Petrov–Galerkin method, moving least squares approximation, magnetoelectric effect, functionally graded material, multiferroic composite

Introduction

The magnetoelectric (ME) coefficient is defined as the ratio of the magnetic (electrical) field output to the electrical (magnetic) input. The ME materials induce the polarization by a magnetic field or vice versa. These materials are promising for wide engineering applications, like magnetic field sensors and magnetically controlled optoelectronic devices. It is most desirable that the ME effect be as large as possible. However, the ME coupling coefficient in single-phase materials is small for principal reasons (Eerenstein et al., 2006). This motivates to study composites of piezoelectric and piezomagnetic media (Bichurin et al., 2003; Feng and Su, 2006; Kuo, 2011; Nan, 1994; Pan et al., 2009; Pan and Wang, 2009). From earlier investigations, it is well known that some composite materials can provide superior properties compared to their virgin monolithic constituent materials. Smith and Shaulov (1985) and Shaulov et al. (1989) found that the piezocomposites have higher piezoelectrical coefficients than their constituents. Analogically one can expect larger ME in composite materials than in monoliths. In composite materials, the ME effect is generated as the product property of a magnetostrictive and a piezoelectric compound. An applied magnetic field induces strain in the magnetostrictive constituent. This is passed on to the piezoelectric constituent, where it induces an electric polarization. In turn, an applied electric field induces a magnetization via the mechanical coupling between the constituents. In contrast to the intrinsic ME effect of single-phase crystalline samples, the composite ME effect manifests predominantly as a nonlinear effect in the applied fields.

A strong ME effect has been recently predicted by Pan and Wang (2009) in artificially fabricated multiferroic composites. It has been shown that the ME response of the laminated composites is determined by four major aspects: (a) the magnetic, electrical, and

[1]Institute of Construction and Architecture, Slovak Academy of Sciences, Bratislava, Slovakia
[2]Department of Civil Engineering, University of Akron, Akron, OH, USA

Corresponding author:
J Sladek, Institute of Construction and Architecture, Slovak Academy of Sciences, 84503 Bratislava, Slovakia.
Email: sladek@savba.sk

mechanical coefficients of the constituents; (b) the respective thickness and number of the piezoelectric and magnetostrictive layers; (c) the type of boundary constituents; and (d) the orientation of the constituents and of the applied electric or magnetic fields. The influence of the thickness ratio for piezomagnetic and piezoelectric layers on the ME was also investigated (Laletin et al., 2008; Shastry et al., 2004; Zhai et al., 2004). The two-dimensional behavior of the laminated magnetoelectroelastic plates is investigated by Heyliger et al. (2004) for two specific geometries: laminates under conditions of cylindrical bending and homogeneous plates under traction-free conditions.

In functionally graded materials (FGMs), the volume fraction of constituents varies in a predominant direction (Miyamoto et al., 1999). Due to their grading feature, FGMs could have many interesting applications in various piezoelectric devices (i.e. Carbonari et al., 2007, 2009, 2010). In this article, we investigate the FGM composite with a pure piezomagnetic behavior on its bottom surface and a pure piezoelectric one on its top surface. Along the plate thickness, the material properties are continuously varying. Both pure constituents have a vanishing ME coefficient. It is an analogical case to previous layered multiferroic composites, only material properties are continuously varying in the FGM composite.

The solution of general boundary value problems for anisotropic magnetoelectroelastic solids requires advanced numerical methods due to the high mathematical complexity. Over the past few years, considerable progress has been made in developing domain or boundary discretization methods. However, the application of these methods to the coupled system brings some difficulties. In recent years, meshless formulations are becoming popular due to their high adaptability and low costs to prepare input and output data in numerical analysis. The moving least squares (MLS) approximation is generally considered as one of the many schemes to interpolate discrete data with a reasonable accuracy. The continuity of the MLS approximation is given by the minimum between the continuity of the basis functions and that of the weight function. So continuity can be tuned to a desired value. In conventional discretization methods, there is a discontinuity of secondary fields (gradients of primary fields) on the interface of elements. In this article, the meshless local Petrov–Galerkin (MLPG) method is developed to solve general boundary value problems. After performing the spatial MLS approximation, a system of ordinary differential equations (ODEs) for certain nodal unknowns is obtained. The Houbolt finite-difference scheme (Houbolt, 1950) is applied for the approximation of the acceleration term in the governing equations for the mechanical field. Various gradation exponents, as well as various boundary conditions, are considered in the numerical analyses.

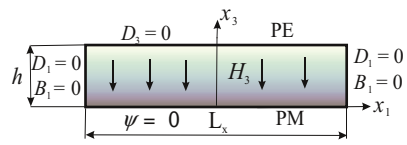

Figure 1. A functionally graded multiferroic plate under given boundary conditions.
PE: piezoelectric; PM: piezomagnetic.

Basic equations

A functionally graded plate made of a multiferroic composite with a pure piezoelectric material on its top surface and a pure piezomagnetic one on its bottom surface is analyzed (Figure 1). Both pure piezoelectric and pure piezomagnetic phases have vanishing ME coefficients. Material properties are assumed to vary continuously along the thickness direction of the plate.

The constitutive equations involving the general magnetoelectroelastic interaction (Nan, 1994) for continuously nonhomogeneous media with spatially dependent material coefficients are given by

$$\sigma_{ij}(\mathbf{x},\tau) = c_{ijkl}(\mathbf{x})\varepsilon_{kl}(\mathbf{x},\tau) - e_{kij}(\mathbf{x})E_k(\mathbf{x},\tau) - d_{kij}(\mathbf{x})H_k(\mathbf{x},\tau) \tag{1}$$

$$D_j(\mathbf{x},\tau) = e_{jkl}(\mathbf{x})\varepsilon_{kl}(\mathbf{x},\tau) + h_{jk}(\mathbf{x})E_k(\mathbf{x},\tau) + \alpha_{jk}(\mathbf{x})H_k(\mathbf{x},\tau) \tag{2}$$

$$B_j(\mathbf{x},\tau) = d_{jkl}(\mathbf{x})\varepsilon_{kl}(\mathbf{x},\tau) + \alpha_{kj}(\mathbf{x})E_k(\mathbf{x},\tau) + \gamma_{jk}(\mathbf{x})H_k(\mathbf{x},\tau) \tag{3}$$

with the strain tensor ε_{ij} being related to the elastic displacements u_i by

$$\varepsilon_{ij} = \frac{1}{2}\left(u_{i,j} + u_{j,i}\right) \tag{4}$$

The constitutive equations relate the elastic strain, the electric field E_i, and the magnetic intensity field H_i to the fields $\{\sigma_{ij}, D_i, B_i\}$, which are the stress tensor, the electric displacement field, and the magnetic induction field, respectively. The elastic coefficient, dielectric permittivity, and magnetic permeability tensors are given by the functional coefficients $c_{ijkl}(\mathbf{x})$, $h_{jk}(\mathbf{x})$, and $\gamma_{jk}(\mathbf{x})$, respectively, while the piezoelectric, piezomagnetic, and ME coefficient tensors are denoted as $e_{kij}(\mathbf{x})$, $d_{kij}(\mathbf{x})$, and $\alpha_{jk}(\mathbf{x})$, respectively. A general variation of material properties with Cartesian coordinates is considered here.

Mechanical waves are significantly slower than the electromagnetic waves for real material coefficients. Then, the electromagnetic fields can be considered like quasi-static (Parton and Kudryavtsev, 1988) and the Maxwell equations are reduced to two scalar equations

$$D_{j,j}(\mathbf{x},\tau) = 0 \tag{5}$$

$$B_{j,j}(\mathbf{x},\tau) = 0 \tag{6}$$

Then, the electric and magnetic intensity vectors can be expressed as gradients of scalar electric and magnetic potentials $\psi(\mathbf{x},\tau)$ and $\mu(\mathbf{x},\tau)$, respectively

$$E_j(\mathbf{x},\tau) = -\psi_j(\mathbf{x},\tau) \tag{7}$$

$$H_j(\mathbf{x},\tau) = -\mu_j(\mathbf{x},\tau) \tag{8}$$

It is assumed that no electric charge exists in the analyzed domain. In the case of some crystal symmetries, one can formulate also the plane-deformation problems (Parton and Kudryavtsev, 1988). Under the plane deformation in the (x_1,x_3)-plane, the constitutive equations (1) to (3) are reduced to the following matrix forms

$$\begin{bmatrix}\sigma_{11}\\ \sigma_{33}\\ \sigma_{13}\end{bmatrix} = \begin{bmatrix} c_{11} & c_{13} & 0\\ c_{13} & c_{33} & 0\\ 0 & 0 & c_{44}\end{bmatrix}\begin{bmatrix}\varepsilon_{11}\\ \varepsilon_{33}\\ 2\varepsilon_{13}\end{bmatrix} - \begin{bmatrix} 0 & e_{31}\\ 0 & e_{33}\\ e_{15} & 0\end{bmatrix}\begin{bmatrix}E_1\\ E_3\end{bmatrix} - \begin{bmatrix} 0 & d_{31}\\ 0 & d_{33}\\ d_{15} & 0\end{bmatrix}\begin{bmatrix}H_1\\ H_3\end{bmatrix} \equiv \mathbf{C}\begin{bmatrix}\varepsilon_{11}\\ \varepsilon_{33}\\ 2\varepsilon_{13}\end{bmatrix} - \mathbf{L}\begin{bmatrix}E_1\\ E_3\end{bmatrix} - \mathbf{K}\begin{bmatrix}H_1\\ H_3\end{bmatrix} \tag{9}$$

$$\begin{bmatrix}D_1\\ D_3\end{bmatrix} = \begin{bmatrix} 0 & 0 & e_{15}\\ e_{31} & e_{33} & 0\end{bmatrix}\begin{bmatrix}\varepsilon_{11}\\ \varepsilon_{33}\\ 2\varepsilon_{13}\end{bmatrix} + \begin{bmatrix} h_{11} & 0\\ 0 & h_{33}\end{bmatrix}\begin{bmatrix}E_1\\ E_3\end{bmatrix} + \begin{bmatrix} \alpha_{11} & 0\\ 0 & \alpha_{33}\end{bmatrix}\begin{bmatrix}H_1\\ H_3\end{bmatrix} \equiv \mathbf{G}\begin{bmatrix}\varepsilon_{11}\\ \varepsilon_{33}\\ 2\varepsilon_{13}\end{bmatrix} + \mathbf{H}\begin{bmatrix}E_1\\ E_3\end{bmatrix} + \mathbf{A}\begin{bmatrix}H_1\\ H_3\end{bmatrix} \tag{10}$$

$$\begin{bmatrix}B_1\\ B_3\end{bmatrix} = \begin{bmatrix} 0 & 0 & d_{15}\\ d_{31} & d_{33} & 0\end{bmatrix}\begin{bmatrix}\varepsilon_{11}\\ \varepsilon_{33}\\ 2\varepsilon_{13}\end{bmatrix} + \begin{bmatrix} \alpha_{11} & 0\\ 0 & \alpha_{33}\end{bmatrix}\begin{bmatrix}E_1\\ E_3\end{bmatrix} + \begin{bmatrix} \gamma_{11} & 0\\ 0 & \gamma_{33}\end{bmatrix}\begin{bmatrix}H_1\\ H_3\end{bmatrix} \equiv \mathbf{R}\begin{bmatrix}\varepsilon_{11}\\ \varepsilon_{33}\\ 2\varepsilon_{13}\end{bmatrix} + \mathbf{A}\begin{bmatrix}E_1\\ E_3\end{bmatrix} + \mathbf{M}\begin{bmatrix}H_1\\ H_3\end{bmatrix} \tag{11}$$

Maxwell's governing equations (5) and (6) have to be supplied by the balance of the momentum

$$\sigma_{ij,j}(\mathbf{x},\tau) + X_i(\mathbf{x},\tau) = \rho\ddot{u}_i(\mathbf{x},\tau) \tag{12}$$

where $\ddot{u}_i$, ρ, and X_i denote the acceleration of elastic displacements, the mass density, and the body force vector, respectively.

MLPG method

To solve the initial-boundary value problems for the considered governing equations, we apply the local integral equation method with meshless approximations. The MLPG method constructs a weak form of the governing equations over the local fictitious subdomains such as Ω_s, which is a small region taken around each node inside the global domain (Atluri, 2004; Sladek et al., 2008). The local subdomains could be of any geometrical shape and size. In this article, the local subdomains are taken to be of a circular shape for simplicity. Applying the Gauss divergence theorem to the local weak form of the governing equation (12), one gets

$$\int_{\partial\Omega_s} \sigma_{ij}(\mathbf{x},\tau)n_j(\mathbf{x})u^*_{ik}(\mathbf{x})d\Gamma - \int_{\Omega_s} \sigma_{ij}(\mathbf{x},\tau)u^*_{ik,j}(\mathbf{x})d\Omega + \int_{\Omega_s} X_i(\mathbf{x},\tau)u^*_{ik}(\mathbf{x})d\Omega = \int_{\Omega_s} \rho(\mathbf{x})\ddot{u}_i(\mathbf{x},\tau)u^*_{ik}(\mathbf{x})d\Omega \tag{13}$$

where $u^*_{ik}(\mathbf{x})$ are the test functions and $\partial\Omega_s$ is the boundary of the local subdomain, which consists of three parts $\partial\Omega_s = L_s \cup \Gamma_{st} \cup \Gamma_{su}$ (Atluri, 2004). Here, L_s is the local boundary that is totally inside the global domain; Γ_{st} is the part of the local boundary, which coincides with the global traction boundary, that is, $\Gamma_{st} = \partial\Omega_s \cap \Gamma_t$; and similarly Γ_{su} is the part of the local boundary that coincides with the global displacement boundary, that is, $\Gamma_{su} = \partial\Omega_s \cap \Gamma_u$.

By choosing a Heaviside step function as the test function $u^*_{ik}(\mathbf{x})$ in each subdomain

$$u^*_{ik}(\mathbf{x}) = \begin{cases} \delta_{ik} \text{ at } \mathbf{x} \in \Omega_s \\ 0 \text{ at } \mathbf{x} \notin \Omega_s \end{cases}$$

The local weak-form equation (13) is converted into the following local boundary-domain integral equations

$$\int_{L_s+\Gamma_{su}} t_i(\mathbf{x},\tau)d\Gamma + \int_{\Omega_s} \rho(\mathbf{x})\ddot{u}_i(\mathbf{x},\tau)d\Omega = -\int_{\Gamma_{st}} \tilde{t}_i(\mathbf{x},\tau)d\Gamma - \int_{\Omega_s} X_i(\mathbf{x},\tau)d\Omega \tag{14}$$

The traction vector $t_i(\mathbf{x},\tau)$ is obtained from the constitutive equation (1)

$$t_i(\mathbf{x},\tau) = \left[c_{ijkl}u_{k,l}(\mathbf{x},\tau) + e_{kij}\psi_k(\mathbf{x},\tau) + d_{kij}\mu_k(\mathbf{x},\tau)\right]n_j(\mathbf{x})$$

Similarly, one can derive the local integral equations corresponding to governing equations (5) and (6)

$$\int_{L_s+\Gamma_{sp}} Q(\mathbf{x},\tau)d\Gamma = -\int_{\Gamma_{sq}} \tilde{Q}(\mathbf{x},\tau)d\Gamma \tag{15}$$

$$\int_{L_s+\Gamma_{sa}} S(\mathbf{x},\tau)d\Gamma = -\int_{\Gamma_{sb}} \tilde{S}(\mathbf{x},\tau)d\Gamma \tag{16}$$

where Γ_{sp}, Γ_{sq}, Γ_{sa}, and Γ_{sb} are parts of the global boundary with prescribed electric potential, the normal component of the electric displacement vector, the magnetic potential, and the normal component of the magnetic induction vector, respectively.

The normal components of the electrical displacement and magnetic induction vectors are defined as

$$\begin{aligned} Q(\mathbf{x},\tau) &= D_j(\mathbf{x},\tau)n_j(\mathbf{x}) \\ &= \left[e_{jkl}u_{k,l}(\mathbf{x},\tau) - h_{jk}\psi_k(\mathbf{x},\tau) - \alpha_{jk}\mu_k(\mathbf{x},\tau)\right]n_j \\ S(\mathbf{x},\tau) &= B_j(\mathbf{x},\tau)n_j(\mathbf{x}) \\ &= \left[d_{jkl}u_{k,l}(\mathbf{x},\tau) - \alpha_{kj}\psi_k(\mathbf{x},\tau) - \gamma_{jk}\mu_k(\mathbf{x},\tau)\right]n_j \end{aligned}$$

The trial functions are approximated by the MLS using a number of nodes spreading over the influence domain. According to the MLS (Belytschko et al., 1996) method, the approximation of the mechanical displacements, electric potential, and magnetic potential can be given as

$$\begin{aligned} \mathbf{u}^h(\mathbf{x},\tau) &= \Phi^T(\mathbf{x})\cdot\hat{\mathbf{u}} = \sum_{a=1}^{n}\phi^a(\mathbf{x})\hat{\mathbf{u}}^a(\tau) \\ \psi^h(\mathbf{x},\tau) &= \sum_{a=1}^{n}\phi^a(\mathbf{x})\hat{\psi}^a(\tau) \\ \mu^h(\mathbf{x},\tau) &= \sum_{a=1}^{n}\phi^a(\mathbf{x})\hat{\mu}^a(\tau) \end{aligned} \tag{17}$$

where the nodal values $\hat{\mathbf{u}}^a(\tau) = \left(\hat{u}_1^a(\tau), \hat{u}_3^a(\tau)\right)^T$, $\hat{\psi}^a(\tau)$, and $\hat{\mu}^a(\tau)$ are fictitious parameters for the displacements, electric potential, and magnetic potential at time τ, respectively, and $\phi^a(\mathbf{x})$ is the shape function associated with the node a.

The number of nodes n used for the approximation is determined by the weight function $w^a(\mathbf{x})$. A fourth-order spline-type weight function is applied in the present work. Then, the C^1-continuity is ensured over the entire domain, and therefore, the continuity conditions of the tractions, electric displacements, and magnetic induction are satisfied.

The traction vectors $t_i(\mathbf{x},\tau)$ at a boundary point $\mathbf{x}\in\partial\Omega_s$ are approximated in terms of the same nodal values $\hat{\mathbf{u}}^a$, $\hat{\psi}^a$, and $\hat{\mu}^a$ as

$$\begin{aligned} \mathbf{t}^h(\mathbf{x},\tau) = \mathbf{N}(\mathbf{x})\mathbf{C}(\mathbf{x})&\sum_{a=1}^{n}\mathbf{B}^a(\mathbf{x})\hat{\mathbf{u}}^a(\tau) \\ &+ \mathbf{N}(\mathbf{x})\mathbf{L}(\mathbf{x})\sum_{a=1}^{n}\mathbf{P}^a(\mathbf{x})\hat{\psi}^a(\tau) \\ &+ \mathbf{N}(\mathbf{x})\mathbf{K}(\mathbf{x})\sum_{a=1}^{n}\mathbf{P}^a(\mathbf{x})\hat{\mu}^a(\tau) \end{aligned} \tag{18}$$

where the matrices $\mathbf{C}(\mathbf{x})$, $\mathbf{L}(\mathbf{x})$, and $\mathbf{K}(\mathbf{x})$ are defined in equation (9), and the matrix $\mathbf{N}(\mathbf{x})$ is related to the normal vector $\mathbf{n}(\mathbf{x})$ on $\partial\Omega_s$ by

$$\mathbf{N}(\mathbf{x}) = \begin{bmatrix} n_1 & 0 & n_3 \\ 0 & n_3 & n_1 \end{bmatrix}$$

and finally, the matrices $\mathbf{B}^a$ and $\mathbf{P}^a$ are represented by the gradients of the shape functions as

$$\mathbf{B}^a(\mathbf{x}) = \begin{bmatrix} \phi_1^a & 0 \\ 0 & \phi_3^a \\ \phi_3^a & \phi_1^a \end{bmatrix}, \mathbf{P}^a(\mathbf{x}) = \begin{bmatrix} \phi_1^a \\ \phi_3^a \end{bmatrix}$$

Similarly, the normal electric displacement $Q(\mathbf{x},\tau)$ can be approximated by

$$\begin{aligned} Q^h(\mathbf{x},\tau) = \mathbf{N}_1(\mathbf{x})\mathbf{G}(\mathbf{x})&\sum_{a=1}^{n}\mathbf{B}^a(\mathbf{x})\hat{\mathbf{u}}^a(\tau) \\ &- \mathbf{N}_1(\mathbf{x})\mathbf{H}(\mathbf{x})\sum_{a=1}^{n}\mathbf{P}^a(\mathbf{x})\hat{\psi}^a(\tau) \\ &- \mathbf{N}_1(\mathbf{x})\mathbf{A}(\mathbf{x})\sum_{a=1}^{n}\mathbf{P}^a(\mathbf{x})\hat{\mu}^a(\tau) \end{aligned} \tag{19}$$

where the matrices $\mathbf{G}(\mathbf{x})$, $\mathbf{H}(\mathbf{x})$, and $\mathbf{A}(\mathbf{x})$ are defined in equation (10) and

$$\mathbf{N}_1(\mathbf{x}) = [\,n_1 \quad n_3\,]$$

Finally, the normal magnetic induction $S(\mathbf{x},\tau)$ is approximated by

$$\begin{aligned} S^h(\mathbf{x},\tau) = \mathbf{N}_1(\mathbf{x})\mathbf{R}(\mathbf{x})&\sum_{a=1}^{n}\mathbf{B}^a(\mathbf{x})\hat{\mathbf{u}}^a(\tau) \\ &- \mathbf{N}_1(\mathbf{x})\mathbf{A}(\mathbf{x})\sum_{a=1}^{n}\mathbf{P}^a(\mathbf{x})\hat{\psi}^a(\tau) \\ &- \mathbf{N}_1(\mathbf{x})\mathbf{M}(\mathbf{x})\sum_{a=1}^{n}\mathbf{P}^a(\mathbf{x})\hat{\mu}^a(\tau) \end{aligned} \tag{20}$$

with the matrices $\mathbf{R}(\mathbf{x})$, $\mathbf{A}(\mathbf{x})$, and $\mathbf{M}(\mathbf{x})$ being defined in equation (11).

Substituting equations (18) to (20) into the local boundary-domain integral equations (14) to (16), one obtains

$$\begin{aligned} &\sum_{a=1}^{n}\left(\int_{L_s+\Gamma_{st}}\mathbf{N}(\mathbf{x})\mathbf{C}(\mathbf{x})\mathbf{B}^a(\mathbf{x})d\Gamma\right)\hat{\mathbf{u}}^a(\tau) \\ &\quad - \sum_{a=1}^{n}\left(\int_{\Omega_s}\rho(\mathbf{x})\phi^a(\mathbf{x})d\Omega\right)\ddot{\hat{\mathbf{u}}}^a(\tau) \\ &\quad + \sum_{a=1}^{n}\left(\int_{L_s+\Gamma_{st}}\mathbf{N}(\mathbf{x})\mathbf{L}(\mathbf{x})\mathbf{P}^a(\mathbf{x})d\Gamma\right)\hat{\psi}^a \end{aligned}$$

$$+ \sum_{a=1}^{n} \left(\int_{L_s + \Gamma_{st}} \mathbf{N}(\mathbf{x})\mathbf{K}(\mathbf{x})\mathbf{P}^a(\mathbf{x}) d\Gamma \right) \hat{\mu}^a(\tau) = -\int_{\Gamma_{st}} \tilde{\mathbf{t}}(\mathbf{x},\tau) d\Gamma - \int_{\Omega_s} \mathbf{X}(\mathbf{x},\tau) d\Omega \tag{21}$$

$$\sum_{a=1}^{n} \left(\int_{L_s + \Gamma_{sq}} \mathbf{N}_1(\mathbf{x})\mathbf{G}(\mathbf{x})\mathbf{B}^a(\mathbf{x}) d\Gamma \right) \hat{\mathbf{u}}^a(\tau) - \sum_{a=1}^{n} \left(\int_{L_s + \Gamma_{sq}} \mathbf{N}_1(\mathbf{x})\mathbf{H}(\mathbf{x})\mathbf{P}^a(\mathbf{x}) d\Gamma \right) \hat{\psi}^a(\tau) - \sum_{a=1}^{n} \left(\int_{L_s + \Gamma_{sq}} \mathbf{N}_1(\mathbf{x})\mathbf{A}(\mathbf{x})\mathbf{P}^a(\mathbf{x}) d\Gamma \right) \hat{\mu}^a(\tau) = -\int_{\Gamma_{sq}} \tilde{Q}(\mathbf{x},\tau) d\Gamma \tag{22}$$

$$\sum_{a=1}^{n} \left(\int_{L_s + \Gamma_{sb}} \mathbf{N}_1(\mathbf{x})\mathbf{R}(\mathbf{x})\mathbf{B}^a(\mathbf{x}) d\Gamma \right) \hat{\mathbf{u}}^a(\tau) - \sum_{a=1}^{n} \left(\int_{L_s + \Gamma_{sb}} \mathbf{N}_1(\mathbf{x})\mathbf{A}(\mathbf{x})\mathbf{P}^a(\mathbf{x}) d\Gamma \right) \hat{\psi}^a(\tau) - \sum_{a=1}^{n} \left(\int_{L_s + \Gamma_{sb}} \mathbf{N}_1(\mathbf{x})\mathbf{M}(\mathbf{x})\mathbf{P}^a(\mathbf{x}) d\Gamma \right) \hat{\mu}^a(\tau) = -\int_{\Gamma_{sb}} \tilde{S}(\mathbf{x},\tau) d\Gamma \tag{23}$$

which are applied to the subdomains that are adjacent to the interior nodes as well as to the boundary nodes on Γ_{st}, Γ_{sq}, and Γ_{sb}.

The discretized essential boundary conditions for displacements, electrical potential, and magnetic potential are satisfied by collocation

$$\sum_{a=1}^{n} \phi^a(\mathbf{x}^b)\hat{\mathbf{u}}^a(\tau) = \tilde{\mathbf{u}}(\mathbf{x}^b,\tau) \quad \text{for } \mathbf{x}^b \in \partial\Omega_s^b \cap \Gamma_u = \Gamma_{su}^b \tag{24}$$

$$\sum_{a=1}^{n} \phi^a(\mathbf{x}^b)\hat{\psi}^a(\tau) = \tilde{\psi}(\mathbf{x}^b,\tau) \quad \text{for } \mathbf{x}^b \in \partial\Omega_s^b \cap \Gamma_p = \Gamma_{sp}^b \tag{25}$$

$$\sum_{a=1}^{n} \phi^a(\mathbf{x}^b)\hat{\mu}^a(\tau) = \tilde{\mu}(\mathbf{x}^b,\tau) \quad \text{for } \mathbf{x}^b \in \partial\Omega_s^b \cap \Gamma_a = \Gamma_{sa}^b \tag{26}$$

The local boundary-domain integral equations (21) to (23) together with the collocation equations (24) to (26) on the global boundary for essential conditions are recast into a complete system of ODEs

$$\mathbf{R}\ddot{\mathbf{x}} + \mathbf{F}\mathbf{x} = \mathbf{Y} \tag{27}$$

where the column vector $\mathbf{x}$ is formed by the nodal unknowns $\{\hat{u}_1^a(\tau), \hat{u}_3^a(\tau), \hat{\psi}^a(\tau), \hat{\mu}^a(\tau)\}$.

The Houbolt method (Houbolt, 1950) is applied for the second order ODE (27), in which the "acceleration" is approximately expressed as

$$\ddot{\mathbf{x}}_{\tau+\Delta\tau} = \frac{2\mathbf{x}_{\tau+\Delta\tau} - 5\mathbf{x}_{\tau} + 4\mathbf{x}_{\tau-\Delta\tau} - \mathbf{x}_{\tau-2\Delta\tau}}{\Delta\tau^2} \tag{28}$$

where $\Delta\tau$ is the time step.

Substituting equation (28) into equation (27), we get the following system of linear algebraic equations for the unknowns $\mathbf{x}_{\tau+\Delta\tau}$

$$\left[\frac{2}{\Delta\tau^2}\mathbf{R} + \mathbf{F}\right]\mathbf{x}_{\tau+\Delta\tau} = \frac{1}{\Delta\tau^2}5\mathbf{R}\mathbf{x}_{\tau} + \mathbf{R}\frac{1}{\Delta\tau^2}\{-4\mathbf{x}_{\tau-\Delta\tau} + \mathbf{x}_{\tau-2\Delta\tau}\} + \mathbf{Y} \tag{29}$$

If a dynamic time-harmonic load is considered, the governing equations are recast into the following form

$$\sigma_{ij,j}(\mathbf{x},\omega) + \rho\omega^2 u_i(\mathbf{x},\omega) = -X_i(\mathbf{x},\omega)$$
$$D_{j,j}(\mathbf{x},\omega) = 0$$
$$B_{j,j}(\mathbf{x},\omega) = 0$$

where ω is the frequency of excitation.

The time-harmonic load is a special case of a more general dynamic load. Therefore, we need to only slightly modify the above local integral equations that are valid in a general case. Then, we can write

$$\sum_{a=1}^{n} \left(\int_{L_s + \Gamma_{st}} \mathbf{N}(\mathbf{x})\mathbf{C}(\mathbf{x})\mathbf{B}^a(\mathbf{x}) d\Gamma \right) \hat{\mathbf{u}}^a(\omega) + \omega^2 \sum_{a=1}^{n} \left(\int_{\Omega_s} \rho(\mathbf{x})\phi^a(\mathbf{x}) d\Omega \right) \hat{\mathbf{u}}^a(\omega) + \sum_{a=1}^{n} \left(\int_{L_s + \Gamma_{st}} \mathbf{N}(\mathbf{x})\mathbf{L}(\mathbf{x})\mathbf{P}^a(\mathbf{x}) d\Gamma \right) \hat{\psi}^a(\omega) + \sum_{a=1}^{n} \left(\int_{L_s + \Gamma_{st}} \mathbf{N}(\mathbf{x})\mathbf{K}(\mathbf{x})\mathbf{P}^a(\mathbf{x}) d\Gamma \right) \hat{\mu}^a(\omega) = -\int_{\Gamma_{st}} \tilde{\mathbf{t}}(\mathbf{x},\omega) d\Gamma - \int_{\Omega_s} \mathbf{X}(\mathbf{x},\omega)(\mathbf{x},\omega) d\Omega \tag{30}$$

$$\sum_{a=1}^{n} \left(\int_{L_s + \Gamma_{sq}} \mathbf{N}_1(\mathbf{x})\mathbf{G}(\mathbf{x})\mathbf{B}^a(\mathbf{x}) d\Gamma \right) \hat{\mathbf{u}}^a(\omega) - \sum_{a=1}^{n} \left(\int_{L_s + \Gamma_{sq}} \mathbf{N}_1(\mathbf{x})\mathbf{H}(\mathbf{x})\mathbf{P}^a(\mathbf{x}) d\Gamma \right) \hat{\psi}^a(\omega) - \sum_{a=1}^{n} \left(\int_{L_s + \Gamma_{sq}} \mathbf{N}_1(\mathbf{x})\mathbf{A}(\mathbf{x})\mathbf{P}^a(\mathbf{x}) d\Gamma \right) \hat{\mu}^a(\omega) = -\int_{\Gamma_{sq}} \tilde{Q}(\mathbf{x},\omega) d\Gamma \tag{31}$$

$$\sum_{a=1}^{n}\left(\int_{L_s+\Gamma_{sb}} \mathbf{N}_1(\mathbf{x})\mathbf{R}(\mathbf{x})\mathbf{B}^a(\mathbf{x})d\Gamma\right)\hat{\mathbf{u}}^a(\omega) - \sum_{a=1}^{n}\left(\int_{L_s+\Gamma_{sb}} \mathbf{N}_1(\mathbf{x})\mathbf{A}(\mathbf{x})\mathbf{P}^a(\mathbf{x})d\Gamma\right)\hat{\psi}^a(\omega) - \sum_{a=1}^{n}\left(\int_{L_s+\Gamma_{sb}} \mathbf{N}_1(\mathbf{x})\mathbf{M}(\mathbf{x})\mathbf{P}^a(\mathbf{x})d\Gamma\right)\hat{\mu}^a(\omega) = -\int_{\Gamma_{sb}} \tilde{S}(\mathbf{x},\omega)d\Gamma \quad (32)$$

Now, the discretized local boundary-domain integral equations are represented by a system of algebraic equations.

Numerical results

The following geometric data for functionally graded multiferroic composite plate are considered in the numerical analysis: length $L_x = 16\,\mathrm{mm}$ and thickness of layers $h = 2\,\mathrm{mm}$. Pure piezoelectric properties corresponding to lead zirconate titanate (PZT)-5A are considered on the top surface of the plate: $c_{11}^T = 99.2\cdot 10^9\,\mathrm{N\,m^{-2}}$, $c_{13}^T = 50.778\cdot 10^9\,\mathrm{N\,m^{-2}}$, $c_{33}^T = 86.856\cdot 10^9\,\mathrm{N\,m^{-2}}$, $c_{44}^T = 21.1\cdot 10^9\,\mathrm{N\,m^{-2}}$, $e_{15}^T = 12.332\,\mathrm{C\,m^{-2}}$, $e_{31}^T = -7.209\,\mathrm{C\,m^{-2}}$, $e_{33}^T = 15.118\,\mathrm{C\,m^{-2}}$, $h_{11}^T = 1.53\cdot 10^{-8}\,\mathrm{C\,(V\,m)^{-1}}$, and $h_{33}^T = 1.5\cdot 10^{-8}\,\mathrm{C\,(V\,m)^{-1}}$.

The material properties on the bottom surface correspond to the piezomagnetic $CoFe_2O_4$: $c_{11}^b = 286\cdot 10^9\,\mathrm{N\,m^{-2}}$, $c_{13}^b = 170.5\cdot 10^9\,\mathrm{N\,m^{-2}}$, $c_{33}^b = 269.5\cdot 10^9\,\mathrm{N\,m^{-2}}$, $c_{44}^b = 45.3\cdot 10^9\,\mathrm{N\,m^{-2}}$, $d_{15}^b = 550\,\mathrm{N\,(A\,m)^{-1}}$, $d_{31}^b = 580.3\,N\,(\mathrm{A\,m})^{-1}$, $d_{33}^b = 699.7\,\mathrm{N\,(A\,m)^{-1}}$, $\gamma_{11}^b = 590\cdot 10^{-6}\,\mathrm{Wb\,(A\,m)^{-1}}$, and $\gamma_{33}^b = 157\cdot 10^{-6}\,\mathrm{Wb\,(A\,m)^{-1}}$.

The mass density for both materials is assumed as $\rho = 7500\,\mathrm{kg/m^3}$. The present computational method is a general numerical approach without any restrictions on the material gradation. The power-law gradation is the simplest material variation, which gives a useful illustration on the influence of the material gradation on the value of the ME coefficient. Therefore, the material properties inside the plate are distributed by a power law

$$f(x_3) = f^b + \left(f^T - f^b\right)\left(\frac{x_3}{h}\right)^n \quad (33)$$

where f^b and f^T correspond to the material coefficient values on the bottom and top surface, respectively. In numerical analyses, we will use various values of the exponent parameter in order to study the dependence of the ME coefficient on the material gradation along x_3. Also various mechanical boundary conditions are considered. We first consider the mechanical traction-free boundary conditions on all the four boundaries of the plate. On lateral sides, vanishing magnetic induction and electric displacements (i.e. their x_1-component) are prescribed. A uniform magnetic potential of -0.1 A and vanishing electric potential are prescribed on the bottom surface of the FGM plate. The electric potential is unknown on the top surface of the FGM layer, where the electrical displacement and magnetic potential are vanishing. To eliminate the rigid-body motion of the plate, the bottom surface at $x_1/L_x = 0.5$ is fixed (i.e. $u_1 = u_3 = 0$), and on the top surface of the composite at $x_1/L_x = 0.5$, we fix $u_1 = 0$. We used 410 (41×10) nodes equidistantly distributed for the MLS approximation of the physical quantities (Figure 2). The local subdomains are considered to be circular with the radius $r_{loc} = 0.0001\,\mathrm{m}$. Stationary boundary value problems are considered first.

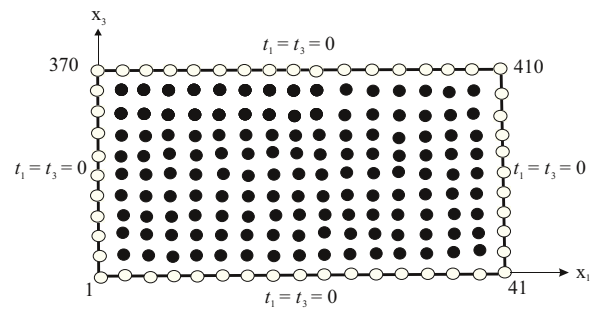

Figure 2. Node distribution and mechanical boundary conditions.

The average intensity of the electric field $\bar{E}_3$ is defined for the FGM composite plate as

$$\bar{E}_3 = \frac{1}{S}\int_S E_3(x_1,x_3)dS \quad (34)$$

where S is the surface of the plate in the $x_1 - x_3$ plane. The average magnetic intensity vector is defined similarly. In the considered sample with $h \ll L_x$, the average magnetic intensity can be assessed as $\bar{H}_3 = 0.1\,\mathrm{A}/0.002\,\mathrm{m} = 50\,\mathrm{A/m}$. Thus, the ME coefficient under vanishing deformations and polarization can be obtained as $\alpha_{33} = h_{33}\alpha'_{33}$, where $\alpha'_{33} = -\bar{E}_3/\bar{H}_3$ is the ME voltage coefficient (Bichurin et al., 2003). Since both the applied magnetic field and the unknown electric field are oriented along the vertical x_3-direction, this is sometimes called the out-of-plane longitudinal ME effect (Bichurin et al., 2003) for layered composites. Similarly, we can define the average ME coefficient in x_1-direction as $\alpha'_{11} = -\bar{E}_1/\bar{H}_1$. The material gradation is assumed in x_3-direction as in the previous case. Now, both the applied magnetic field and the unknown electric field are oriented along the horizontal x_1-direction; therefore, this effect is sometimes called the in-plane longitudinal ME effect (Bichurin et al., 2003). Since the material coefficients are invariable in the x_1-direction, the average magnetic intensity $\bar{H}_1$ can

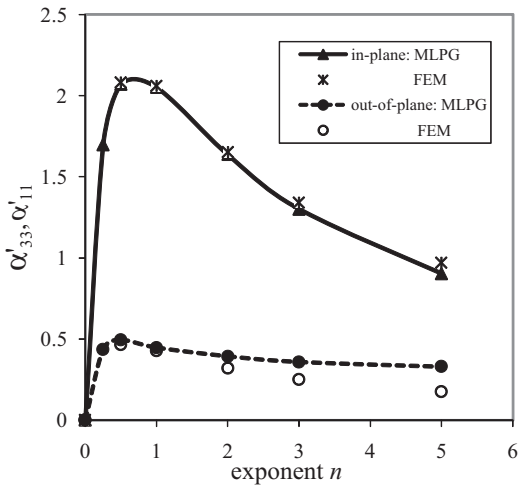

Figure 3. Variation of the ME voltage coefficients (in V/A) on the gradation exponent n in the plate with mechanical traction-free boundaries on all the boundaries.
ME: magnetoelectric; MLPG: meshless local Petrov–Galerkin; FEM: finite element method.

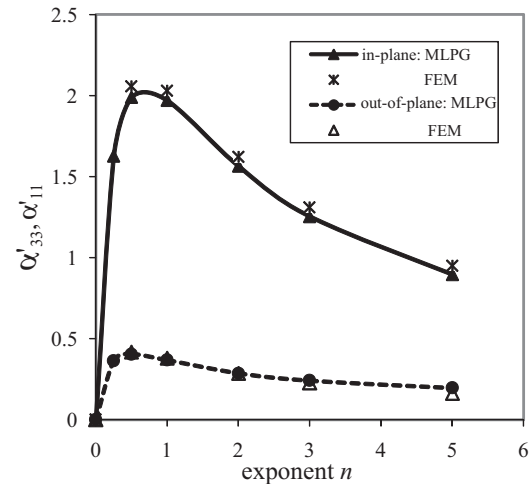

Figure 4. Variation of the ME voltage coefficients on the gradation exponent n in the plate with fixed bottom surface $u_3 = 0$ (traction in x_1-direction along the bottom surface is still free).
ME: magnetoelectric; MLPG: meshless local Petrov–Galerkin; FEM: finite element method.

be assessed as $\bar{H}_1 = 0.8\,\mathrm{A}/0.016\,\mathrm{m} = 50\,\mathrm{A/m}$, provided that the constant magnetic potential $\mu = 0.8\,\mathrm{A}$ is prescribed on the right lateral side ($x_1 = 0.016\,\mathrm{m}$) and on the left lateral side $\mu = 0$. The electric potential on the left lateral side and the electrical displacement on the right lateral side are vanishing. The mechanical displacement $u_1 = 0$ is fixed on the left lateral side. The calculated dependences of both the out-of-plane (α'_{33}) and in-plane (α'_{11}) ME voltage coefficients on the gradation exponent n are presented in Figure 3, as compared to those based on the finite element method (FEM) calculations, with the unit of the ME voltage coefficient being V/A. The FEM results were obtained by the COMSOL computer code with 500 linear elements.

One can observe that the maximum ME coefficient values are at exponent value of about 0.5. The in-plane ME coefficient α'_{11} is significantly larger than the out-of-plane ME coefficient α'_{33}. Recently, Pan and Wang (2009) observed a similar phenomenon for layered multiferroic composites, where the in-plane ME coefficient was about 2 times larger than the out-of-plane one. In considered FGM multiferroic composites, we can see more enhanced in-plane ME coefficient. One can also observe from Figure 3 that there is a good agreement between the MLPG and FEM results for α'_{11} coefficient in the whole n interval. However, a certain discrepancy between the MLPG and FEM results for α'_{33} occurs when the gradation exponent n becomes large. Probably 10 elements along x_3 is not sufficient for an accurate modeling of larger material gradients by FEM since in the FEM analysis, the material properties on each element are considered to be uniform. In the MLPG, on the other hand, no such approximation is required, and the actual material gradation is considered.

In the next numerical example, we analyze the same plate with other mechanical boundary conditions on the bottom surface. In this case, the elastic displacement in x_3-direction is fixed, while the specimen in the x_1-direction is traction free. Both the ME coefficients calculated by the proposed MLPG are presented in Figure 4 as compared to the FEM results. From Figures 3 and 4, we can see that different mechanical boundary conditions have only slight influence on the ME coefficients and that the in-plane ME coefficients are about five times larger than the out-of-plane ME coefficients.

In the third case, we consider the clamped boundary conditions on the bottom surface. That is, both displacement components are vanishing there. The ME coefficients are presented in Figure 5 together with the results calculated by the FEM. Again the influence of the material gradation on the ME coefficients is similar in all three mechanical boundary conditions on the bottom surface of the FGM plate. The peak value of the out-of-plane ME coefficients is slightly larger for the clamped condition than in previous cases. Furthermore, in this case, the agreement between the FEM and MLPG results for both ME voltage coefficients is very good.

In previous numerical examples, we considered a pure magnetic load on the FGM multiferroic plate. In the next example, a combined magnetomechanical load is applied. On the top surface, a uniform tension $\sigma_{33} = 10^5\,\mathrm{Pa}$ is applied. The bottom surface is fixed in the normal direction ($u_3 = 0$) but free in the tangential

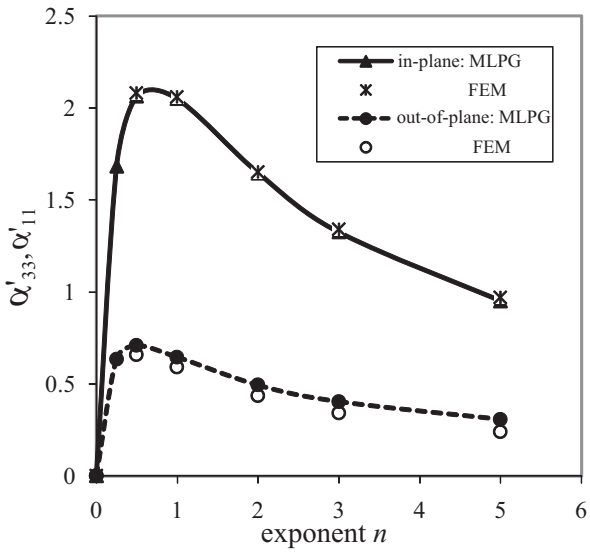

Figure 5. Variation of the ME voltage coefficients on the gradation exponent n in the plate with clamped bottom surface.
ME: magnetoelectric; MLPG: meshless local Petrov–Galerkin; FEM: finite element method.

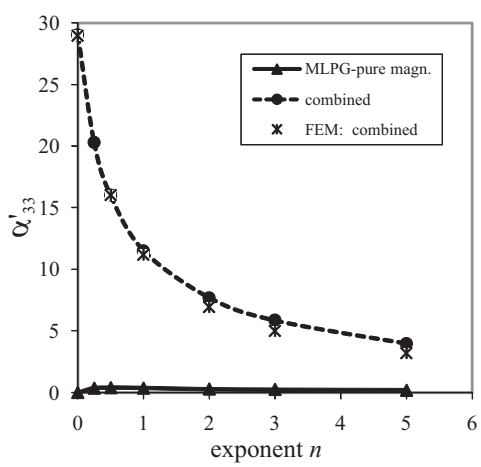

Figure 6. Influence of a combined load on the out-of-plane ME voltage coefficient in the FGM plate with fixed normal elastic displacement on the bottom surface ($u_3 = 0$).
FGM: functionally graded material; ME: magnetoelectric; MLPG: meshless local Petrov–Galerkin; FEM: finite element method.

direction. Simultaneously, the FGM plate is under the magnetic load with prescribed magnetic potential $\mu = -0.1$ A on its bottom surface and vanishing magnetic potential on the top surface. The dependence of the ME coefficients on the gradation exponent in the plate under the pure magnetic and combined loads is presented in Figure 6. It is observed clearly that the ME coefficient can be significantly increased if the combined magnetomechanical load is applied to the plate.

A combined magnetomechanical load with harmonic variation in time is considered in the next numerical

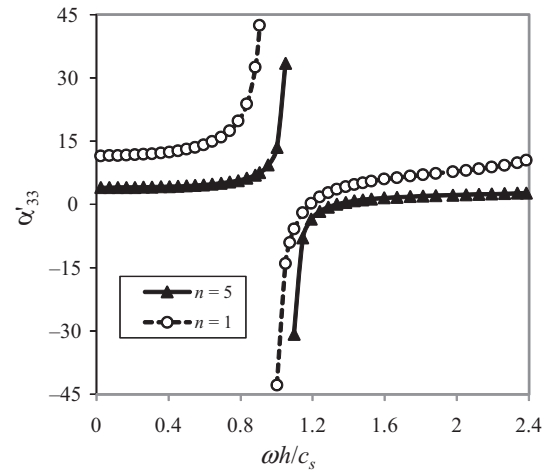

Figure 7. The ME voltage coefficient versus frequency.
ME: magnetoelectric.

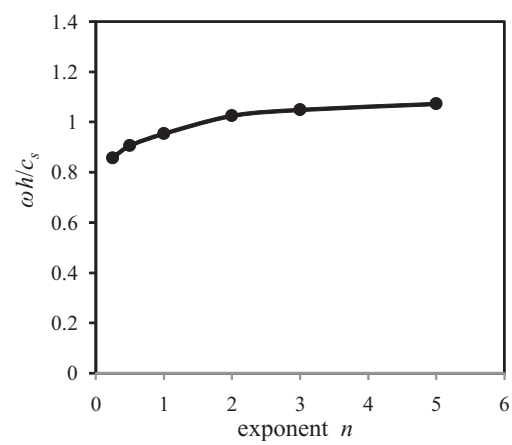

Figure 8. Variation of the resonance frequency versus the gradation exponent.

example. Various frequencies are used in the analyses for the FGM plate with fixed bottom surface ($u_3 = 0$) but vanishing shear traction. The normalized frequency $\omega h/c_s$ is used with $c_s = \sqrt{c_{44}/\rho}$. The analyses are performed for two different material gradations $n = 1$ and 5. The out-of-plane ME coefficient is presented in Figure 7. It is observed from Figure 7 that (a) the resonance frequency for $n = 5$ is slightly larger than that for $n = 1$, (b) the ME coefficient for $n = 1$ is larger than that for $n = 5$ (in terms of the algebraic value), and (c) in the vicinity to the resonance frequency, one can tune the ME coefficient to a larger value.

The variation of the resonance frequency for the FGM multiferroic plate on the gradation exponent is presented in Figure 8. The resonance frequency increases slightly if the gradation exponent increases. Notice that the volume fraction of the piezomagnetic material is larger than the piezoelectric one if the gradation exponent n is larger than 1.

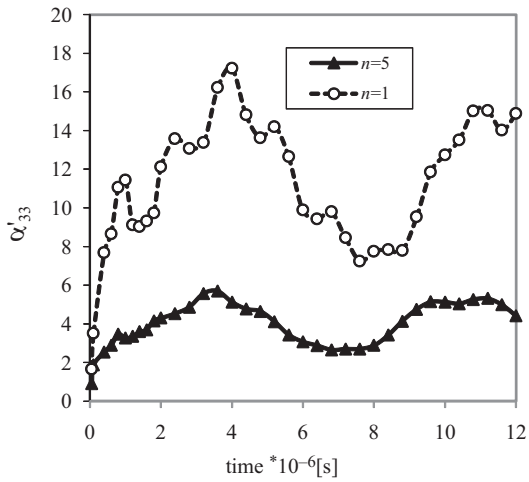

Figure 9. The ME voltage coefficient for the FGM plate under an impact mechanical load and stationary magnetic intensity H_3. ME: magnetoelectric; FGM: functionally graded material.

Finally, the combined magnetomechanical loading is considered with the mechanical load being given as the Heaviside time step. Again, the bottom surface of the plate is fixed in the normal direction ($u_3 = 0$) but free in the tangential direction. All other boundary conditions are the same as in the previous example. Time variation of the out-of-plane ME coefficient is presented in Figure 9. It is noted from Figure 9 that the peak values for the gradation factor $n = 1$ are about 3 times larger than those for $n = 5$, similar to the trend for the corresponding static case where the ME coefficient for $n = 1$ is larger than that for $n = 5$, as shown in Figure 4.

Conclusion

An MLPG is applied to investigate the ME coefficients for functionally graded composite plate composed of piezoelectric and piezomagnetic phases. Static, time-harmonic, and transient dynamic conditions are considered. Both a pure magnetic intensity load and a combined magnetomechanical load are applied to the plate. The material properties on the bottom surface have a pure piezomagnetic behavior, and on the top surface, they are pure piezoelectric. Along the plate thickness, the material coefficients are continuously varying according to the power law with various gradation exponents. The magnetic intensity or mechanical load causes deformations in the piezomagnetic constituent of the FGM composite. The composite plate deformations induce electric potential in the piezoelectric constituent of the FGM composite. Under an optimal gradation of the piezoelectric or piezomagnetic constituents, we can significantly enhance the ME coefficient.

The influence of the mechanical boundary conditions on the in-plane and out-of-plane ME coefficients is investigated. The influence of the fixed bottom surface of the plate is small on the coefficient value with respect to the traction-free boundary conditions. The in-plane coefficient is significantly larger than the out-of-plane one. It follows from numerical analyses that optimal gradation is for exponent $n = 0.5$ in power-law gradient composites with ferromagnetic and ferroelectric phases. It corresponds to the case where there is a significant material gradation close to the bottom surface with pure piezomagnetic properties.

The mechanical load condition can significantly enhance the ME effect. The ME coefficient linearly increases with increasing mechanical load if linear magnetoelectroelasticity is used. Numerical simulations enable understanding the behavior of the functionally graded multiferroic composite plates. This is a great challenge to design smart structures with an optimal ME coefficient.

Acknowledgement

The authors acknowledge the support by the Slovak Science and Technology Assistance Agency registered under number APVV-0014-10. The authors also gratefully acknowledge the financial assistance of the European Regional Development Fund (ERDF) under the Operational Programme Research and Development/Measure 4.1 Support of networks of excellence in research and development as the pillars of regional development and support to international cooperation in the Bratislava region/Project No. 26240120020 Building the centre of excellence for research and development of structural composite materials–2nd stage.

References

Atluri SN (2004) *The Meshless Method (MLPG) for Domain and BIE Discretizations*. Forsyth: Tech Science Press.

Belytschko T, Krongauz Y, Organ D, et al. (1996) Meshless methods: an overview and recent developments. *Computer Methods in Applied Mechanics and Engineering* 139: 3–47.

Bichurin MI, Petrov VM and Srinivasan G (2003) Theory of low-frequency magnetoelectric coupling in magnetostrictive-piezoelectric bilayers. *Physical Review B* 68: 054402.

Carbonari RC, Paulino GH and Silva ECN (2010) Integral piezoactuator system with optimum placement of functionally graded material—a topology optimization paradigm. *Journal of Intelligent Materials and Systems Structures* 21: 1653–1668.

Carbonari RC, Silva ECN and Paulino GH (2007) Topology optimization design of functionally graded bimorph-type piezoelectric actuators. *Smart Materials and Structures* 16: 2605–2620.

Carbonari RC, Silva ECN and Paulino GH (2009) Multi-actuated functionally graded piezoelectric micro-tools design: a multiphysics topology optimization approach. *International Journal for Numerical Methods in Engineering* 77: 301–336.

Eerenstein W, Mathur ND and Scott JF (2006) Multiferroic and magnetoelectric materials. *Nature* 442: 759–765.

Feng WJ and Su RKL (2006) Dynamic internal crack problem of a functionally graded magneto-electro-elastic strip. *International Journal of Solids Structures* 43: 5196–5216.

Heyliger P, Ramirez F and Pan E (2004) Two-dimensional static fields in magnetoelectroelastic laminates. *Journal of Intelligent Materials Systems and Structures* 15: 689–709.

Houbolt JC (1950) A recurrence matrix solution for the dynamic response of elastic aircraft. *Journal of Aeronautical Sciences* 17: 371–376.

Kuo HY (2011) Multicoated elliptic fibrous composites of piezoelectric and piezomagnetic phases. *International Journal of Engineering Science* 49: 561–575.

Laletin VM, Petrov VM, Tuskov DS, et al. (2008) Frequency dependence of the magnetoelectric effect in ceramic composites based on lead zirconate titanate and nickel ferrite. *Technical Physics Letters* 34: 83–89.

Miyamoto Y, Kaysser WA, Rabin BH, et al. (1999) *Functionally Graded Materials*: *Design, Processing and Applications*. Boston, MA: Kluwer Academic Publishers.

Nan CW (1994) Magnetoelectric effect in composites of piezoelectric and piezomagnetic phases. *Physical Review B* 50: 6082–6088.

Pan E and Wang R (2009) Effects of geometric size and mechanical boundary conditions on magnetoelectric coupling in multiferroic composites. *Journal of Physics D* 42: 245503.

Pan E, Wang X and Wang R (2009) Enhancement of magnetoelectric effect in multiferroic fibrous nanocomposites via size-dependent material properties. *Applied Physics Letters* 95: 181904.

Parton VZ and Kudryavtsev BA (1988) *Electromagnetoelasticity, Piezoelectrics and Electrically Conductive Solids*. New York: Gordon and Breach Science Publishers.

Shastry S, Srinivasan G, Bichurin MI, et al. (2004) Microwave magnetoelectric effects in single crystal bilayers of yttrium iron garnet and lead magnesium niobate-lead titanate. *Physical Review B* 70: 064416.

Shaulov AA, Smith WA and Ting RY (1989) Modified-lead-titanate/polymer composites for hydrophone applications. *Ferroelectrics* 93: 177–182.

Sladek J, Sladek V, Solek P, et al. (2008) Fracture analysis of cracks in magneto-electro-elastic solids by the MLPG. *Computational Mechanics* 42: 697–714.

Smith WA and Shaulov AA (1985) Tailoring the properties of composite piezoelectric materials for medical ultrasonic transducers. *IEEE Ultrasonic Symposium* 2: 642–647.

Zhai JY, Cai N, Shi Z, et al. (2004) Coupled magnetoelectric properties of laminated $PbZr_{0.53}Ti_{0.47}O_3/NiFe_2O_4$ ceramics. *Journal of Applied Physics* 95: 5685.